ELSEVIER

0141-1187(95)00009-7

Applied Ocean Research 17 (1995) 205–216
Published by Elsevier Science Limited
Printed in Great Britain
0141-1187/95/$09.50

Dynamic loss of stability in depth control of submersible vehicles

Fotis A. Papoulias, Craig A. Bateman & Selcuk Ornek
Naval Postgraduate School, Department of Mechanical Engineering, Monterey, CA 93943, USA

(Received 6 October 1994; accepted 8 May 1995)

Control of a modern submarine is a multi-dimensional dynamical problem coupling considerations of initial static stability, hydrodynamic performance, and control system response. In this work, the loss of stability at moderate-to-high speeds is examined using a nonlinear Hopf bifurcation analysis. Complete linear state feedback is used for demonstration purposes for depth control at level attitude and for a fixed nominal speed. The control time constant, the nominal and actual speeds, the metacentric height, and the stern-to-bow-plane ratio are used as the main bifurcation parameters. A complete local bifurcation mapping provides a systematic method for evaluating the bounds of controllability for the control system design parameters for a vehicle with a given set of hydrodynamic coefficients. The submarine and its potential design modifications are verified with direct numerical simulations.

NOMENCLATURE

a	Dummy independent variable
a_0	Steady-state value of a
$\mathbf{A}$	Linearized matrix of the system in its nominal state
$b(x)$	Local beam of the hull
C_D	Quadratic drag coefficient
I_y	Vehicle mass's moment of inertia
k_1, k_2, k_3, k_4	Controller gains in θ, w, q and z, respectively
m	Vehicle mass
M	Pitch moment
M_a	Derivative of M with respect to a
q	Pitch rate
T	Period of oscillation
$\mathbf{T}$	Matrix of eigenvectors of $\mathbf{A}$ evaluated at the bifurcation point
T_C	Control time constant
U	Vehicle's forward speed
U_C	Critical value of U
U_0	Nominal forward speed
w	Heave velocity
$\mathbf{x}$	State variable vector, $\mathbf{x} = [\theta, w, q, z]$
(x_B, z_B)	Body-fixed coordinates of vehicle's center of buoyancy
(x_G, z_G)	Body-fixed coordinates of vehicle's center of gravity
x_{GB}	Center of gravity/center of buoyancy separation, $x_G - x_B$
z	Deviation off the commanded depth
$\mathbf{z}$	State variable vector in canonical form
z_1, z_2	Critical variables of $\mathbf{z}$
z_3, z_4	Stable coordinates of $\mathbf{z}$
z_{GB}	Vehicle metacentric height, $z_G - z_B$
Z	Heave force
Z_a	Derivative of Z with respect to a

Greek symbols

α	Bow-plane-to-stern-plane deflection ratio
α_i	Center manifold expansion coefficients of z_3
β_i	Center manifold expansion coefficients of z_4
θ	Vehicle pitch angle
δ_b	Bow plane deflection
δ_s, δ	Stern plane deflection
δ'	Stern plane angle including saturation
δ_{sat}	Saturation value of δ
ω_0	Imaginary part of eigenvalues at the bifurcation point

1 INTRODUCTION

The fundamental goal of submarine control is to reach and maintain the ordered depth. Any design that does not meet this goal, in the face of the inherent complexities, is

not overly useful in a practical vessel. Current evaluation schemes involve extensive model testing and system identification.[1] The end result is usually a set of coefficients that describe, in terms of a polynomial regression, the hydrodynamic force and moment on the hull.[2] Although this representation is adequate for most ordinary maneuvers, the ultimate goal is to develop an analytical method to determine the stability and performance of a potential design. Much work has been done on depth control and modeling of submarines in the vertical plane.[3–7] The stability of a particular design has a significant impact on its responsiveness. A vehicle with a large margin of stability will not be very responsive. The problem becomes one of determining how close to the margins we can get without a total loss of stability. By expanding the scope of our research to include nonlinear terms, we are able to define the limits of stability and therefore the margins. Nonlinear dynamics and bifurcation theory provides us with the tools for solving this problem.[8,9]

At low forward speeds, a submersible using stern planes for attitude and depth control can experience a loss of stability in the form of stern planes reversal.[10] This is a pitchfork bifurcation that can be predicted[11] and can be accounted for in the control design. The purpose of this work is to develop a methodology for evaluating the limits of stability for a submarine at moderate-to-high speeds. Once these limits are mapped, the nature of the loss of stability must be determined. For this we use a Hopf bifurcation analysis which consists of third-order Taylor series expansions,[12] center manifold approximations,[13] and integral averaging.[14,15] After the stability limits are determined, we are able to define the control system design parameters and evaluate the controllability of the design. Vehicle modeling in this work follows standard notation,[16] while full linear state feedback is used for demonstration purposes to achieve depth control.[17] Numerical results are presented for the DARPA SUBOFF vehicle, for which a set of hydrodynamic coefficients and geometric properties is available.[1] All results are shown in standard dimensionless form with respect to vehicle length $L = 4.26$ m, and nominal speed.

2 PROBLEM FORMULATION

2.1 Equations of motion

Assuming that vehicle motion is restricted in the vertical plane, the mathematical model consists of the coupled nonlinear heave and pitch equations of motion. In a moving coordinate frame fixed at the vehicle's geometrical center, Newton's equations of motion for a port/starboard symmetric vehicle are expressed as follows

$$\begin{aligned} &m(\dot{w} - Uq - z_G q^2 - x_G \dot{q}) \\ &= Z_{\dot{q}}\dot{q} + Z_{\dot{w}}\dot{w} + Z_q Uq + Z_w Uw \\ &\quad - C_D \int_{\text{tail}}^{\text{nose}} b(x) \frac{(w - xq)^3}{|w - xq|}\, dx \\ &\quad + (W - B)\cos\theta + U^2(Z_{\delta_s}\delta_s + Z_{\delta_b}\delta_b) \end{aligned} \tag{1}$$

$$\begin{aligned} &I_y\dot{q} + mz_G wq - mx_G(\dot{w} - Uq) \\ &= M_{\dot{q}}\dot{q} + M_{\dot{w}}\dot{w} + M_q Uq + M_w Uw \\ &\quad - C_D \int_{\text{tail}}^{\text{nose}} b(x) \frac{(w - xq)^3}{|w - xq|} x\, dx \\ &\quad - (x_G W - x_B B)\cos\theta - (z_G W - z_B B)\sin\theta \\ &\quad + U^2(M_{\delta_s}\delta_s + M_{\delta_b}\delta_b) \end{aligned} \tag{2}$$

In eqns (1) and (2), W is the vehicle weight, B the buoyancy, $(x_G,\ z_G)$ the coordinates of the center of gravity, $(x_B,\ z_B)$ the coordinates of the center of buoyancy, δ_s the stern plane angle, and δ_b the bow plane angle. The cross-flow integral terms in the above equations become important during hovering operations or low-speed maneuvering, whereas at high speeds, U (and consequently low angles of attack with respect to the water), their effect is minimal. The drag coefficient, C_D, is assumed to be constant along the entire vehicle length for simplicity. This does not significantly affect the results that follow. The remaining symbols in eqns (1) and (2) follow standard notation and are explained in the Nomenclature. It should be noted that the symbol U in this work designates the constant forward speed along the vehicle's longitudinal axis, and not the resultant vehicle speed.

The vehicle pitch rate is

$$\dot{\theta} = q \tag{3}$$

and the rate of change of depth is

$$\dot{z} = -U\sin\theta + w\cos\theta \tag{4}$$

where θ is the pitch angle with respect to the nominal horizontal direction. The vehicle's geometry and definitions for most of the above symbols are shown in Fig. 1. The forward velocity U is assumed to be kept constant by the propulsion control system during depth keeping. Any changes in U are assumed to take place in a quasi-steady way, i.e. at a rate much slower than the vehicle's motion in the dive plane.

2.2 Control law

Equations (1)–(4) can be written as a set of four nonlinear coupled differential equations in the form

$$\dot{\theta} = q \tag{5}$$

$$\begin{aligned} \dot{w} = {} & a_{11}Uw + a_{12}Uq + a_{13}z_{GB}\sin\theta + b_{11}U^2\delta_s \\ & + b_{12}U^2\delta_b + d_w(w,\ q) + c_1(w,\ q) \end{aligned} \tag{6}$$

$$\dot{q} = a_{21}Uw + a_{22}Uq + a_{23}z_{GB}\sin\theta + b_{21}U^2\delta_s$$

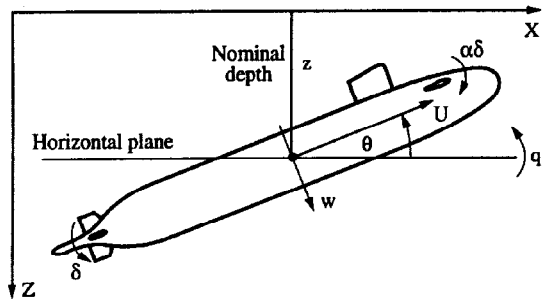

Fig. 1. Vehicle geometry and definitions of symbols.

$$+ b_{22}U^2\delta_b + d_q(w, q) + c_2(w, q) \tag{7}$$

$$\dot{z} = -U\sin\theta + w\cos\theta \tag{8}$$

where

$$\begin{aligned}
D_v &= (m - Z_{\dot{w}})(I_y - M_{\dot{q}}) \\
&\quad - (mx_G + Z_{\dot{q}})(mx_G + M_{\dot{w}}) \\
a_{11}D_v &= (I_y - M_{\dot{q}})Z_w + (mx_G + Z_{\dot{q}})M_w \\
a_{12}D_v &= (I_y - M_{\dot{q}})(m + Z_q) \\
&\quad + (mx_G + Z_{\dot{q}})(M_q - mx_G) \\
a_{13}D_v &= -(mx_G + Z_{\dot{q}})W \\
b_{11}D_v &= (I_y - M_{\dot{q}})Z_{\delta_s} + (mx_G + Z_{\dot{q}})M_{\delta_s} \\
b_{12}D_v &= (I_y - M_{\dot{q}})Z_{\delta_b} + (mx_G + Z_{\dot{q}})M_{\delta_b} \\
a_{21}D_v &= (m - Z_{\dot{w}})M_w + (mx_G + M_{\dot{w}})Z_w \\
a_{22}D_v &= (m - Z_{\dot{w}})(M_q - mx_G) \\
&\quad + (mx_G + M_{\dot{w}})(m + Z_q) \\
a_{23}D_v &= -(m - Z_{\dot{w}})W \\
b_{21}D_v &= (m - Z_{\dot{w}})M_{\delta_s} + (mx_G + M_{\dot{w}})Z_{\delta_s} \\
b_{22}D_v &= (m - Z_{\dot{w}})M_{\delta_b} + (mx_G + M_{\dot{w}})Z_{\delta_b} \\
d_w(w, q)D_v &= (I_y - M_{\dot{q}})I_w + (mx_G + Z_{\dot{q}})I_q \\
d_q(w, q)D_v &= (m - Z_{\dot{w}})I_q + (mx_G + M_{\dot{w}})I_w \\
c_1(w, q)D_v &= (I_y - M_{\dot{q}})mz_Gq^2 - (mx_G + Z_{\dot{q}})mz_Gwq \\
c_2(w, q)D_v &= -(m - Z_{\dot{w}})mz_Gwq + (mx_G + M_{\dot{w}})mz_Gq^2
\end{aligned}$$

In eqns (5)–(8), the vehicle is assumed to be neutrally buoyant ($W = B$), level ($x_G = x_b$), and statically stable ($z_G > z_b$). The terms I_w and I_q represent the cross-flow drag integrals in eqns (1) and (2), and $z_{GB} = z_G - z_b$ is the metacentric height. Without loss of generality, we can assume z_b to be zero, so that $z_{GB} = z_G$.

During most cruising operations, effective depth control can be achieved by using the linearized version of eqns (5)–(8), where the linearization is performed around a level flight path at the commanded depth. The linear system of equations then used for depth control law design is:

$$\dot{\theta} = q \tag{9}$$

$$\dot{w} = a_{11}U_0w + a_{12}U_0q + a_{13}z_{GB}\theta + b_1U_0^2\delta \tag{10}$$

$$\dot{q} = a_{21}U_0w + a_{22}U_0q + a_{23}z_{GB}\theta + b_2U_0^2\delta \tag{11}$$

$$\dot{z} = -U_0\theta + w \tag{12}$$

where U_0 is the nominal speed for gain selection, α is defined as the bow-plane-to-dive-plane deflection ratio, and we have denoted

$$\begin{aligned}
\delta_s &= \delta \\
\delta_b &= \alpha\delta \\
b_1 &= b_{11} + \alpha b_{12} \\
b_2 &= b_{21} + \alpha b_{22}
\end{aligned} \tag{13}$$

A linear full state feedback control law has the form[17]

$$\delta = k_1\theta + k_2w + k_3q + k_4z \tag{14}$$

where the gains k_1, k_2, k_3, k_4 are computed such that the closed-loop system [eqns (9)–(14)] has the desired dynamics. If the desired characteristic equation has the general form

$$\lambda^4 + \alpha_3\lambda^3 + \alpha_2\lambda^2 + \alpha_1\lambda + \alpha_0 = 0 \tag{15}$$

the controller gains can be computed by equating coefficients of the actual and desired characteristic equations,

$$b_1U_0^2k_2 + b_2U_0^2k_3 = -\alpha_3 - (a_{11} + a_{22})U_0 \tag{16}$$

$$\begin{aligned}
&b_2U_0^2k_1 + (b_2a_{12} - b_1a_{22})U_0^3k_2 \\
&\quad + (b_1a_{21} - b_2a_{11})U_0^3k_3 + b_1U_0^2k_4 \\
&= -\alpha_2 - a_{23}z_{GB} + (a_{11}a_{22} - a_{21}a_{12})
\end{aligned} \tag{17}$$

$$\begin{aligned}
&(b_2a_{11} - b_1a_{21})U_0^3k_1 \\
&\quad + (b_1a_{23} - b_2a_{13})z_{GB}U_0^2k_2 \\
&\quad + (b_2 + b_1a_{22} - b_2a_{12})U_0^3k_4 \\
&= \alpha_1 + (a_{13}a_{21} - a_{23}a_{11})z_{GB}U_0
\end{aligned} \tag{18}$$

$$\left[(b_1a_{21} - b_2a_{11})U_0^4 + (b_1a_{23} - b_2a_{13})z_{GB}U_0^2\right]k_4 = \alpha_0 \tag{19}$$

The coefficients α_i are selected such that the desired characteristic eqn (15) has real and negative roots located at $-1/T_C$. Therefore, T_C is the effective time constant of the depth regulator system under nominal conditions.

3 STABILITY

3.1 Bifurcation analysis

In system dynamics, the classical definition of stability states that the real parts of all eigenvalues of the system must be negative. Therefore, our initial investigations into the stability of the model were to find those eigenvalues whose real parts cross the imaginary axis. We concentrate

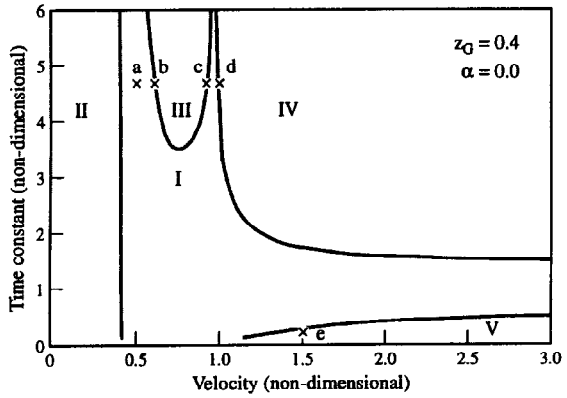

Fig. 2. A typical bifurcation map showing the five distinct regions.

on the crossing of the imaginary axis here, since real axis crossing has been studied extensively.[11] The linearized set of state equations [eqns (9)–(12)] is compactly written in the form $\dot{\mathbf{x}} = \mathbf{A}\mathbf{x} + \mathbf{B}\delta$, where $\mathbf{x}$ is the four-dimensional state variables vector $[\theta, w, q, z]$ and $\delta = -\mathbf{K}\mathbf{x}$ is the state feedback control law as defined in eqn (14). The eigenvalues of the system at speeds other than nominal are found by solving

$$\det |\mathbf{A} - \mathbf{B}\mathbf{K} - s\mathbf{I}| = 0 \tag{20}$$

In eqn (20), $\mathbf{K}$ is the gain vector defined in eqn (14), and s is the Laplace transformation variable. In the local bifurcation analysis, a pseudo-root-locus method is employed where the time constant, T_C, is fixed. The constant T_C fixes the placement of the system poles at a given nominal forward speed, U_0. The actual speed, U, is then varied incrementally with the system eigenvalues calculated at each speed increment. When the real part of an eigenvalue changes sign between the limits of a speed increment, a bisection method is employed to find the speed where the real part of the eigenvalue equals zero. For each point where the real part of an eigenvalue crosses the imaginary axis, the associated T_C and critical speed U_C are plotted on a bifurcation map. This map delineates the regions of linear stability from the regions of instability. A family of bifurcation maps were generated by varying the nominal speed, U_0, initial stability, z_{GB}, and control surface gain, α.

3.2 Typical results and simulations

Figure 2 shows a typical bifurcation map with its five distinct regions. Region I is the area of linear stability. In region II, there is one real positive eigenvalue which is indicative of a pitchfork bifurcation as explained in Papoulias and Riedel.[11] Regions III, IV and V have at least one pair of complex conjugate eigenvalues with a positive real part. This indicates that unstable oscillatory behavior is expected from the model in these regions.

An extensive set of simulations were run to verify the bifurcation map's prediction of system stability.[18] While the results of the simulations showed the demarcation between the stable and unstable regions, the simulations also demonstrated that the linear bifurcation analysis failed to predict the method of departure from stability. Five points, a–e, as shown in Fig. 2, were chosen to illustrate the model's behavior in the regions of interest. The first four points a–d correspond to the same control time constant $T_C = 4.75$ dimensionless seconds. Table 1 lists the eigenvalues found at each of these points and Table 2 shows the eigenvalues associated with the exact bifurcation point near points b, c and d. Note that the eigenvalues are given in dimensional terms, while all other information in the tables are non-dimensionalized.

Point a is in the region of stability and simulations show a rapid convergence to nominal depth. The agreement between the predicted and observed period of oscillation, T, is also very good. The predicted period of oscillation is based on the imaginary part of the critical pair of eigenvalues, and it is equal to 2π divided by the imaginary part. This corresponds to a zeroth-order approximation of the actual period of oscillation, as predicted by the center manifold theorem.[8] The approximation is valid for parameter values close to the bifurcation point. The critical pair of eigenvalues is that with the maximum real part, and non-dimensionalized with respect to vehicle length and actual speed, U. The small differences in the predicted periods of oscillation in Tables 1 and 2 are due to the different speeds used in the non-dimensionalization. Small-amplitude oscillatory motions were observed at the unstable points, b and c, with periods well predicted from the linearized results. The case of point d is different, however. The amplitude of the oscillatory response was found to be considerable larger in this case, while the predicted period of oscillation was approximately twice the observed value, as shown in Table 1. The dominant limit cycle period at about 80 s is associated with the creation of the limit cycle at the exact bifurcation point as shown in Table 2. This shows that, in general, the oscillatory component of the response of a nonlinear system should be evaluated not at the parameter point of interest, but at the closest bifurcation point instead. Finally, a simulation run at point e demonstrated an unbounded departure from the nominal with no visible oscillatory component. It is evident, therefore, that a more detailed investigation of the mechanism of loss of stability has to be undertaken.

4 HOPF BIFURCATIONS

4.1 Introduction

By definition, a Hopf bifurcation occurs when a pair of complex conjugate eigenvalues cross into the right-hand half plane. When this occurs, the system will deviate from a steady-state solution in an oscillatory manner.

Table 1. Eigenvalues and periods of points shown in Fig. 2

Points	Eigenvalues	U	Measured T	Predicted T
a	$-0.4581, -0.0001, -0.0515 \pm 0.4938$	$0.50U_0$	4.13	5.00
b	$-0.6226, -0.0003, 0.0052 \pm 0.4463$	$0.62U_0$	5.59	5.62
c	$-0.5888, -0.0046, 0.0067 \pm 0.2983$	$0.94U_0$	12.86	12.75
d	$-0.3000 \pm 0.2889, 0.0387 \pm 0.0268$	$1.03U_0$	80.00	155.4
e	$-27.890, -1.7300, 0.7100 \pm 4.1700$	$1.50U_0$	NA	1.46

Table 2. Eigenvalues and periods of the exact bifurcation points associated with the points shown in Fig. 2

Points	Eigenvalues	U_C	Measured T	Predicted T
b	$-0.6070, -0.0002, 0.0000 \pm 0.4506$	$0.61U_0$	6.11	5.57
c	$-0.5710, -0.0054, 0.0000 \pm 0.2884$	$0.93U_0$	13.13	13.18
d	$-0.2675 \pm 0.2063, 0.0000 \pm 0.0558$	$1.02U_0$	74.93	74.67

This deviation is typically either supercritical or subcritical. For the supercritical case, stable limit cycles form after straight-line stability is lost. Assume that a certain parameter, $w(x)$, is varying quasi-statically. When the independent variable x is less than a critical value, x_{crit}, all eigenvalues of the system are located in the left-hand half plane and the system is nominally stable. At $x = x_{crit}$, a complex conjugate pair moves into the right-hand half plane and forms a stable limit cycle. As the distance $D = w(x) - w(x_{crit})$ increases, the amplitude of the limit cycle will also increase. If D remains small then the system will remain near the nominal steady-state solution.

In the subcritical case, unstable limit cycles are generated prior to the critical point being reached. Thus, as $w(x)$ approaches $w(x_{crit})$, the system could deviate from the nominal steady-state solution and converge to a large-amplitude limit cycle before the nominal system loses stability. Here, a random disturbance can cause a nominally stable system to exhibit oscillatory behavior. Once $w(x)$ equals $w(x_{crit})$, the nominal system becomes unstable and a discontinuous increase in the amplitude of oscillation is seen. A system design must make a distinction between these two types of bifurcation because of the disparate nature of stability loss. Thus, the designer cannot rely on a linear approximation and must use higher-order approximations of the equations of motion to adequately analyze the dynamic system.

4.2 Third-order approximations

The nonlinear equations of motion are expanded using a third-order Taylor series approximation near the nominal steady state, $\mathbf{x} = [0]$. The control law is then modeled as,

$$\delta' = \delta_{sat} \tanh\left(\frac{\delta}{\delta_{sat}}\right) \tag{21}$$

where δ_{sat} is the saturation angle of the control plane input. Equation (21) exhibits similar behavior to the frequently used hard saturation function, with the added advantage of the analyticity properties which are required for the following Taylor series expansions. Using the same approximation for the control law as the equations of motion, δ' becomes

$$\delta' = \delta - \frac{1}{3\delta_{sat}^2}\delta^3 \tag{22}$$

Therefore, the state equations can now be written as

$$\dot{\mathbf{x}} = \mathbf{A}\mathbf{x} + \mathbf{g}(\mathbf{x}) \tag{23}$$

where

$$\mathbf{x} = [\theta,\ w,\ q,\ z]^T \tag{24}$$

and the higher order terms are

$$g_1 = 0 \tag{25}$$

$$g_2 = b_1 U^2 \delta_3(\theta,\ w,\ q,\ z) - \frac{1}{6}a_{13}z_{GB}\theta^3 + c_{11}q^2 + c_{12}wq \tag{26}$$

$$g_3 = b_2 U^2 \delta_3(\theta,\ w,\ q,\ z) - \frac{1}{6}a_{23}z_{GB}\theta^3 + c_{21}wq + c_{22}q^2 \tag{27}$$

$$g_4 = -\frac{1}{2}w\theta^2 + \frac{1}{6}U\theta^3 \tag{28}$$

The term δ_3 contains the third-order expansion terms derived from substituting δ into δ'.

Defining $\mathbf{T}$ as the matrix of eigenvectors of $\mathbf{A}$ evaluated at the Hopf bifurcation point, the transformation

$$\mathbf{x} = \mathbf{T}\mathbf{z} \tag{29}$$

transforms the system into a canonical form,

$$\dot{\mathbf{z}} = \mathbf{T}^{-1}\mathbf{A}\mathbf{T}\mathbf{z} + \mathbf{T}^{-1}\mathbf{g}(\mathbf{T}\mathbf{z}) \tag{30}$$

At the bifurcation point

$$\mathbf{T}^{-1}\mathbf{A}\mathbf{T} = \begin{vmatrix} 0 & -\omega_0 & 0 & 0 \\ \omega_0 & 0 & 0 & 0 \\ 0 & 0 & p & 0 \\ 0 & 0 & 0 & q \end{vmatrix} \tag{31}$$

with $\omega_0 > 0$ and $p, q < 0$. The coordinates z_3 and z_4 correspond to the negative eigenvalues p and q and are

asymptotically stable. Center manifold theory[8] states that the stable coordinates z_3, z_4 can be expressed as polynomials in the critical coordinates z_1, z_2 and this relationship is at least second order. Therefore, we can write

$$z_3 = \alpha_1 z_1^2 + \alpha_2 z_1 z_2 + \alpha_3 z_2^2 \tag{32}$$

and

$$z_4 = \beta_1 z_1^2 + \beta_2 z_1 z_2 + \beta_3 z_2^2 \tag{33}$$

The coefficients α_i, β_i can be computed as follows. We differentiate eqns (32) and (33) with respect to $\mathbf{z}$

$$\dot{z}_3 = 2\alpha_1 z_1 \dot{z}_1 + \alpha_2(\dot{z}_1 z_2 + z_1 \dot{z}_2) + 2\alpha_3 z_2 \dot{z}_2$$

$$\dot{z}_4 = 2\beta_1 z_1 \dot{z}_1 + \beta_2(\dot{z}_1 z_2 + z_1 \dot{z}_2) + 2\beta_3 z_2 \dot{z}_2$$

and substitute $\dot{z}_1 = -\omega_0 z_2$, and $\dot{z}_2 = \omega_0 z_1$. Therefore

$$\dot{z}_3 = \alpha_2 \omega_0 z_1^2 + 2(\alpha_3 - \alpha_1)\omega_0 z_1 z_2 - \alpha_2 \omega_0 z_2^2 \tag{34}$$

and

$$\dot{z}_4 = \beta_2 \omega_0 z_1^2 + 2(\beta_3 - \beta_1)\omega_0 z_1 z_2 - \beta_2 \omega_0 z_2^2 \tag{35}$$

The third and fourth equations of (30) are written as

$$\begin{bmatrix} \dot{z}_3 \\ \dot{z}_4 \end{bmatrix} = \begin{bmatrix} p & 0 \\ 0 & q \end{bmatrix} \begin{bmatrix} z_3 \\ z_4 \end{bmatrix} + [D] \tag{36}$$

where,

$$[D] = \mathbf{T}^{-1}\mathbf{g}_2(\mathbf{Tz})$$

and $\mathbf{g}_2(\mathbf{Tz})$ contains the second-order terms of $\mathbf{g}(\mathbf{Tz})$. We substitute eqns (32) and (33) into eqn (36) and equate coefficients with eqns (34) and (35). In this way we get a linear system of equations in α_i and β_i. From this we can write the two-dimensional state space equations as

$$\dot{z}_1 = -\omega_0 z_2 + r_{11} z_1^3 + r_{12} z_1^2 z_2 + r_{13} z_1 z_2^2 + r_{14} z_2^3 + p_{11} z_1^2 + p_{12} z_1 z_2 + p_{13} z_2^2 \tag{37}$$

and

$$\dot{z}_2 = \omega_0 z_1 + r_{21} z_1^3 + r_{22} z_1^2 z_2 + r_{23} z_1 z_2^2 + r_{24} z_2^3 + p_{21} z_1^2 + p_{22} z_1 z_2 + p_{23} z_2^2 \tag{38}$$

where the coefficients r_{ij} and p_{ij} are derived from eqn (30).

These equations are only valid exactly at the Hopf bifurcation point. For speeds U in a region near the bifurcation point, the equations become

$$\dot{z}_1 = \alpha' \epsilon z_1 - (\omega_0 + \omega' \epsilon) z_2 + F_1(z_1, z_2) \tag{39}$$

and

$$\dot{z}_2 = (\omega_0 + \omega' \epsilon) z_1 + \alpha' \epsilon z_2 + F_2(z_1, z_2) \tag{40}$$

where α', ω' are the derivatives with respect to U of the real and imaginary parts of the critical complex conjugate pair of eigenvalues evaluated at the bifurcation point; ϵ is the difference in U from the critical value U_C; and the nonlinear functions F_1 and F_2 are

$$F_1 = r_{11} z_1^3 + r_{12} z_1^2 z_2 + r_{13} z_1 z_2^2 + r_{14} z_2^3 + p_{11} z_1^2 + p_{12} z_1 z_2 + p_{13} z_2^2 \tag{41}$$

and

$$F_2 = r_{21} z_1^3 + r_{22} z_1^2 z_2 + r_{23} z_1 z_2^2 + r_{24} z_2^2 + p_{21} z_1^2 + p_{22} z_1 z_2 + p_{23} z_2^2 \tag{42}$$

Transforming z_1 and z_2 to polar coordinates of the form

$$z_1 = R \cos \Theta \tag{43}$$

$$z_2 = R \sin \Theta \tag{44}$$

eqns (39) and (40) become

$$\dot{R} = \alpha' \epsilon R + F_1(R, \Theta) \cos \Theta + F_2(R, \Theta) \sin \Theta \tag{45}$$

and

$$R\dot{\Theta} = (\omega + \omega' \epsilon) R + F_2(R, \Theta) \cos \Theta - F_1(R, \Theta) \sin \Theta \tag{46}$$

Equation (45) then yields

$$\dot{R} = \alpha' \epsilon R + P(\Theta) R^3 + Q(\Theta) R^2 \tag{47}$$

By averaging eqn (47) over one cycle, we can obtain an equation with constant coefficients. Defining

$$K = \frac{1}{2\pi} \int_0^{2\pi} P(\Theta)\ \mathrm{d}\Theta \tag{48}$$

and

$$L = \frac{1}{2\pi} \int_0^{2\pi} Q(\Theta)\ \mathrm{d}\Theta \tag{49}$$

and carrying out the indicated integrations, we obtain

$$L = 0 \tag{50}$$

and

$$K = \frac{1}{8}(3r_{11} + r_{13} + r_{22} + 3r_{24}) \tag{51}$$

which reduces eqn (47) to

$$\dot{R} = \alpha' \epsilon R + K R^3 \tag{52}$$

The existence and stability of the limit cycles is determined by analyzing the equilibrium points of the averaged eqn (52), which correspond to periodic solutions in z_1 and z_2 as seen in the coordinate transformation eqns (43) and (44). From eqn (52) we can see that two conditions exist:

(1) If $\alpha' > 0$, then:
   (a) if $K > 0$, unstable limit cycles coexist with the stable equilibrium for $\epsilon < 0$; or

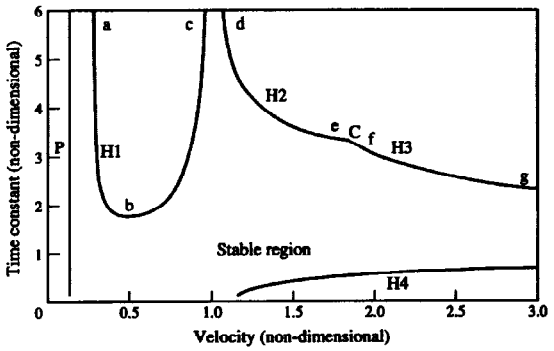

Fig. 3. A typical bifurcation map for the model.

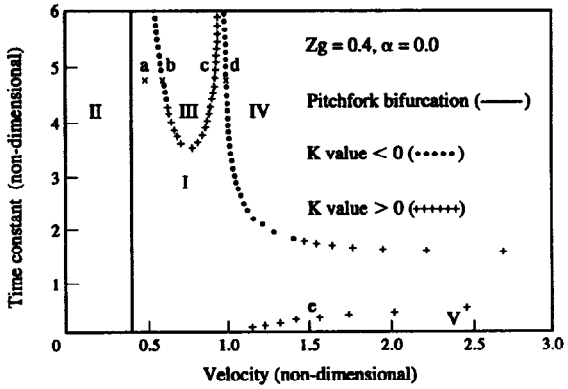

Fig. 4. A plot of the stability coefficient K associated with Fig. 2.

(b) if $K < 0$, stable limit cycles coexist with the unstable equilibrium for $\epsilon > 0$.

(2) If $\alpha' < 0$, then:

(a) if $K > 0$, unstable limit cycles coexist with the stable equilibrium for $\epsilon > 0$; or

(b) if $K < 0$, stable limit cycles coexist with the unstable equilibrium for $\epsilon < 0$.

Based on these criteria, by computing the nonlinear stability coefficient K we can use it to distinguish between the two different types of Hopf bifurcation:

- supercritical if $K < 0$; and
- subcritical if $K > 0$.

4.3 Results

A typical bifurcation map for the SUBOFF model is shown in Fig. 3. This map is characterized by the pitchfork curve (P) and the three Hopf bifurcation curves (H1, H2 and H3). The nature of curve P has been previously analyzed[15] and those results are reconfirmed in this study.

Curve H1 is characterized by a weak supercritical branch (a → b) at low nominal speeds, U_0. As U_0 increases, this branch develops a weak-to-moderate subcritical behavior with K between 0 and 10^2. The second branch of H1 (b → c) has a consistent moderate subcritical behavior with K of the order of 10^2. The cusp point (C) marks the intersection of curve H2 with curve H3. The cusp is highly dependent on both U_0 and the initial stability z_{GB}. For a given U_0, as z_{GB} increases, curve H2 (d → e) shifts from a very weak subcritical nature with K between 10^{-2} and 1 to a very weak supercritical nature with K between -1 and -10^{-2}. With a lower U_0 and/or higher z_{GB}, point e moves down in the time constant and may not intersect curve H3. Curve H3 (f → g) is a strong supercritical bifurcation with K values between -10^4 and -10^6. The position of H3 is independent of U_0, the initial stability, and the control surface coordination gain, α. Finally, curve H4 is a strong subcritical branch with K having values between 10^3 and 10^6. Because of this highly subcritical behavior, H4 can dominate and obscure the stable region at speeds greater than $U/U_0 = 1$.

Figure 4 plots the K values for the representative bifurcation map shown in Fig. 2. Note the predicted supercritical and subcritical branches associated with Fig. 3. Point a is inside the stable region (I) and numerical simulations converge to zero. Point b is located in the unstable region, immediately after a supercritical bifurcation. As a result, small-amplitude limit cycle oscillations have developed. The same is true as we move towards point c, although we expect a family of unstable limit cycles around this point as a result of the subcritical bifurcation. As we approach point d, a family of stable limit cycles is generated but its behavior is influenced by the previously developed unstable limit cycles. The real part of the critical pair of eigenvalues is becoming positive and relatively large, which means that the amplitudes of these stable limit cycles are expected to be significantly higher, a result which was confirmed by numerical simulations.[18] The imaginary parts of the critical pair of eigenvalues are also changing very fast in this region. This means that the period of these limit cycles must be computed based on the value of the imaginary part right at the bifurcation point, rather than its value at the specific parameter point. Point e is in the strongly subcritical region V, thus we see the rapid divergence from stability also observed in numerical simulations.

4.4 Simulations

The response of the system was simulated using an Adams–Bashforth integration scheme, the control law [eqn (14)] and control gains [eqn (16)–(19)]. The nondimensional ship speed U, control time constant T_C, nominal speed U_0, initial stability z_{GB}, and control surface coordination gain α were used as parameter values. A nominal 0.03 m/s vertical speed was used as the external initial disturbance in all calculations. The simulations

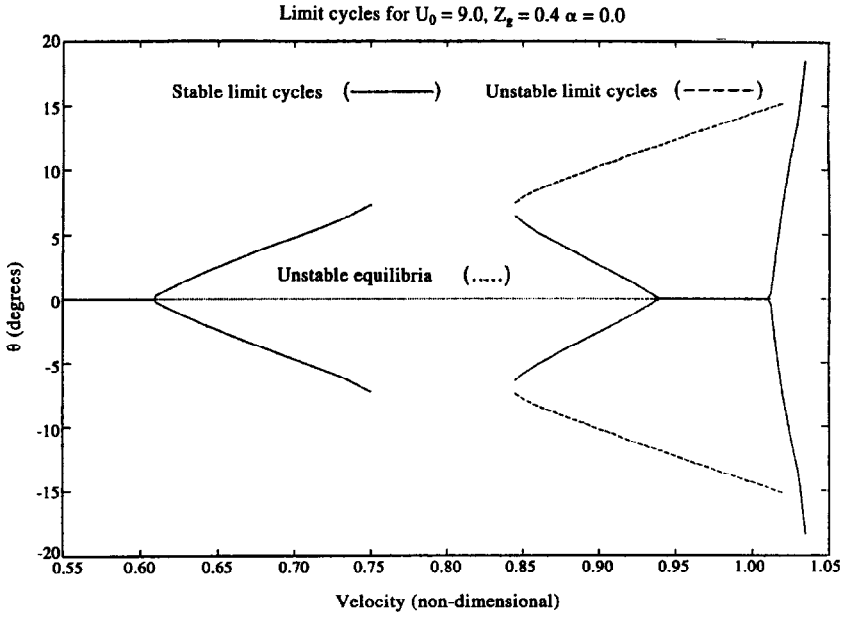

Fig. 5. Amplitude response for a speed range encompassing the Hopf bifurcation points shown in Fig. 2.

were used to compare the Hopf bifurcation data in two ways:

(1) by confirming the subcritial/supercritical behavior predicted by the values of K; and
(2) by comparing the predicted to the simulated period of oscillation.

In Fig. 5, we have plotted the stable and unstable equilibria and limit cycle amplitudes from our example first used in Fig. 2. Figure 5 clearly shows the observed subcritical or supercritical behavior according to the predictions based on the values of K. The important features to note in Fig. 5 are:

(1) the unstable limit cycles found with the subcritical Hopf bifurcation;
(2) the divergence of the amplitudes as the velocity moves away from the bifurcation critical speed; and
(3) the rapid divergence of the right-most bifurcation and its quick and abrupt termination.

To see why the abrupt termination occurs we must look at the root locus plot, parametrized by the speed U, as shown in Fig. 6. This third Hopf bifurcation persists only for a small range of forward speeds. Soon after the pair of complex conjugate eigenvalues crosses the imaginary axis, a break-in to the real axis occurs. The pair of complex conjugate eigenvalues with positive real parts splits into two positive eigenvalues, one of which is increasing while the other one moves towards zero. The periodic solutions gradually change their morphology into a form of relaxation oscillations.[19] In this case, the trajectories spend most of their time in the vicinity of slowly varying divergent solutions followed by abrupt changes. The solutions quickly exceed physically realizable values of pitch angle and in practice the limit cycles cease to exist.

5 APPLICATIONS

5.1 Control parameters

From the typical bifurcation maps we can see that a region of stability is created between the pitchfork and Hopf bifurcation boundaries. For the control system designer, the limits of the parameters must be defined prior to starting the design. By maximizing the region of stability, we can give the designer the most leeway in his work. There are three parameters that we can use to change the bifurcation maps in this study, namely nominal speed, initial stability, and control surface coordination coefficient.

Figure 7 summarizes the effects of changing the nominal speed, U_0. Three curves for nominal speeds of 0.9, 2.7 and 4.5 m/s are shown. We can see that although the pitchfork line moves to the left, in dimensional speeds this line remains nearly constant with a dimensional stern plane reversal occurring at 1.2 knots. The high-speed Hopf boundaries ($U/U_0 > 1$) move apart as the nominal speed increases. The effectiveness of increasing U_0 is limited in the upper branch by the fixed position of the H3 curve with the maximum practical T_C achieved at U_0 = 2.7 m/s. In the lower arm there is no increase in the stability area after U_0 = 2.7 m/s, therefore any increase in U_0 offers no advantage. For the low-speed Hopf curves ($U/U_0 < 1$) we quickly lose our margin of stability as U_0 increases thus necessitating further changes to regain the lost area of stability.

Figure 8 shows the effect of increasing the metacentric height, z_{GB} from 3 to 12 cm. The subcritical H4 branch remains constant while the upper high-speed Hopf branch moves down effectively decreasing the area of stability.

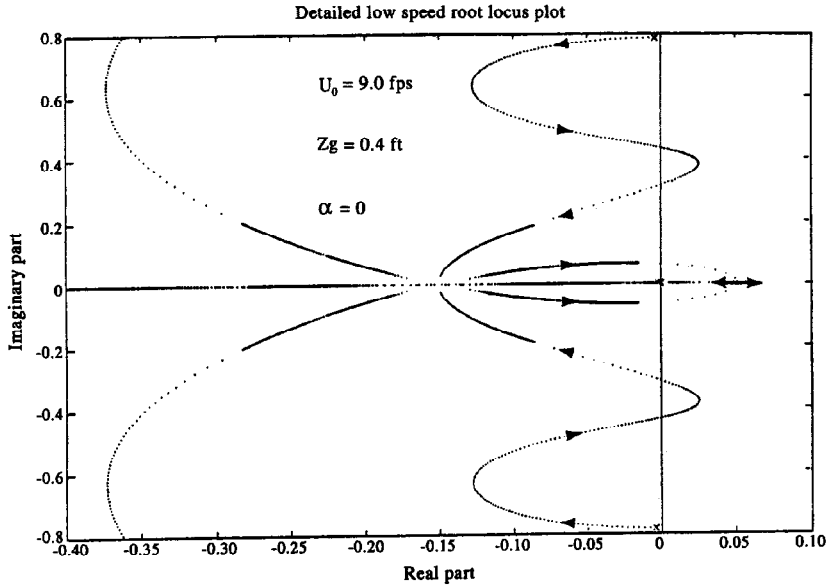

Fig. 6. Root-locus plot of the eigenvalues associated with Fig. 5.

The low-speed Hopf curves move up to increase the low-speed area of stability. We can see that the additional loss in area is by the movement of the pitchfork line to the right. At z_{GB} = 12 cm, stern plane reversal occurs at a dimensional speed of 2.4 knots, which is well within the currently accepted range of 1.0–3.0 knots for modern submarines. Therefore, it is desirable to balance the initial stability, z_{GB}, to maximize the low- and high-speed areas.

An increase in the control surface coordination coefficient, α, is shown in Fig. 9. We recall (see Fig. 1) that $\alpha = 0$ implies no bow plane activity, whereas $\alpha = 1$ implies maximum bow plane activity moving in the opposite direction to the stern planes to yield maximum pitching moment. Note that the low- and high-speed Hopf curves all move up in T_C. While the low-speed Hopf curves give a large increase in stability, the high-speed curves move up proportionally and there is no increase in the stable area. This allows the designer to shift the range of stable time constants without a loss of high-speed stability. The pitchfork line moves to the left until it equals zero for $\alpha = 1$.

In order to examine what happens at the extremes of the design options we can look at the low nominal speed (0.9 m/s) bifurcation maps. Figure 10 shows a typical bifurcation map such as the one we have previously discussed. As the metacentric height is increased, there are significant changes in the nature of the bifurcation curves. In Fig. 11 we see that the pitchfork line has moved significantly to the right and has intersected the low-speed Hopf bifurcation curve. This intersection along with the merger of the H2 and H4 curves has combined to reduce the region of stability to a negligible portion of the map.

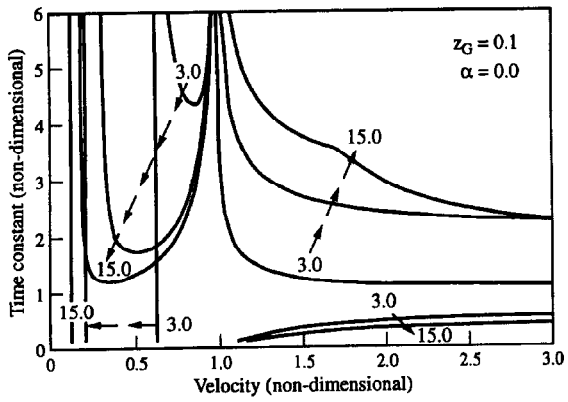

Fig. 7. The effect of changing the nominal speed, U_0, on the bifurcation maps.

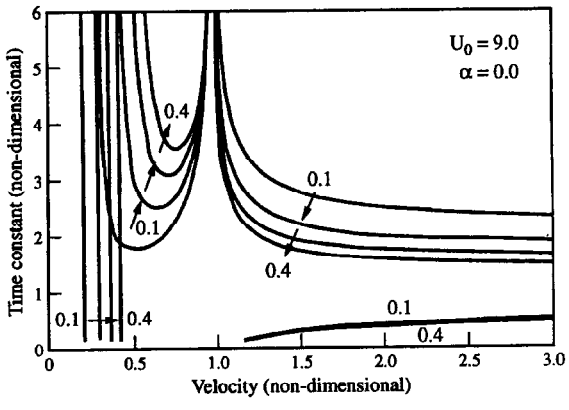

Fig. 8. The effect of changing the initial stability, z_{GB}, on the bifurcation maps.

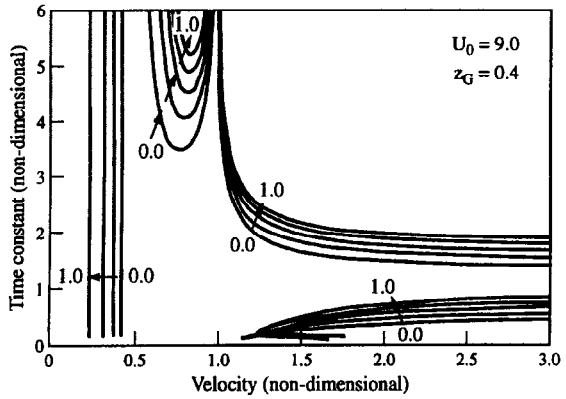

Fig. 9. The effect of changing the control surface coordination coefficient, α, on the bifurcation maps.

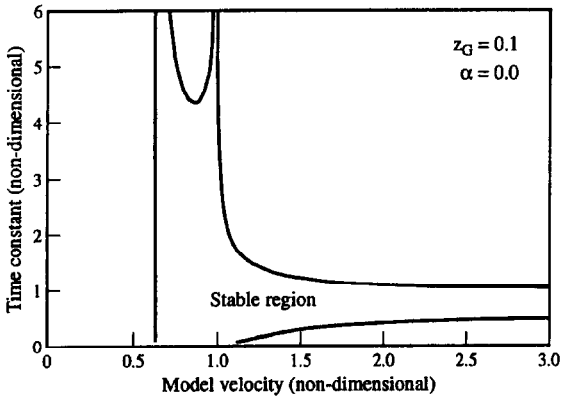

Fig. 10. A low nominal speed bifurcation map.

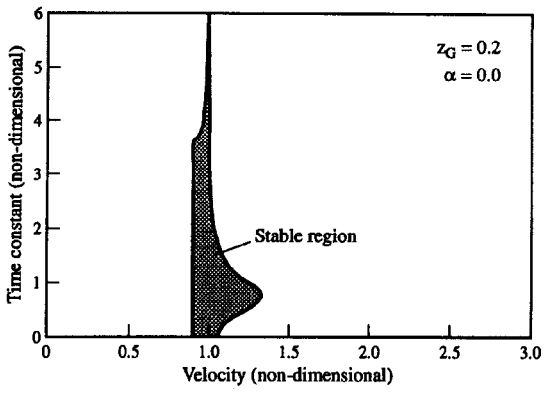

Fig. 11. The effect of an increase in the metacentric height for low nominal speeds.

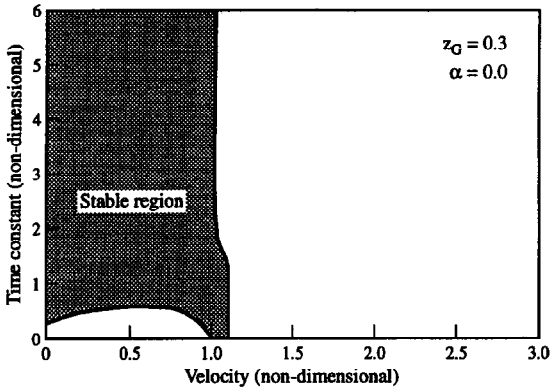

Fig. 12. The transition from supercritical to subcritical pitchfork bifurcation.

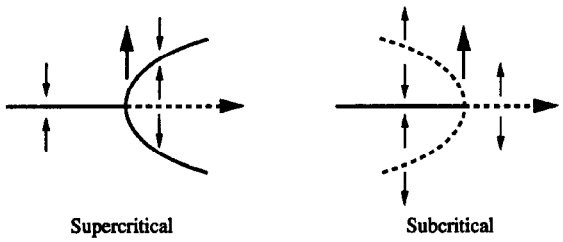

Fig. 13. Schematic representation of supercritical and subcritical pitchfork bifurcations.

A further increase in the metacentric height, as shown in Fig. 12, demonstrates a dramatic change in the nature of the stability of the model. The low-speed region has two hyperbola-like Hopf bifurcation curves (the upper curve occurs well above the region of interest) bounding the lower and upper limits of stability. For speeds $U/U_0 > 1$, the pitchfork bifurcation line now intersects the H2 curve and has changed from a supercritical to a subcritical pitchfork. In the supercritical pitchfork, stable secondary solutions branch out after the primary solution becomes unstable, as in the case of Euler beam buckling.[9] In the subcritical case, however, the secondary solutions are unstable and exist (locally) in the parameter region where the primary solution is still stable. Therefore the system tends to be very sensitive to imperfections and external disturbances, as in the case of the buckling of arcs. Random disturbances of sufficient magnitude can destabilize the system even though the primary equilibrium state is still theoretically stable. This shows that although initial stability is necessary for overall stability, if the metacentric height becomes too large it can have an adverse effect on the performance of the submarine.

5.2 Design evaluation

All computations up to this point have been performed with fixed values of the force and moment coefficients of the control surfaces. Linear bifurcation methods fail to predict a change in the system response for changes in control surface coefficients. The bifurcation maps are exactly the same for a 10:1 range of the control surface coefficients, from 0.1× to 1.0×. In other words, the bifurcation points are independent of the size and effectiveness of the control surfaces. Therefore, we must either resort

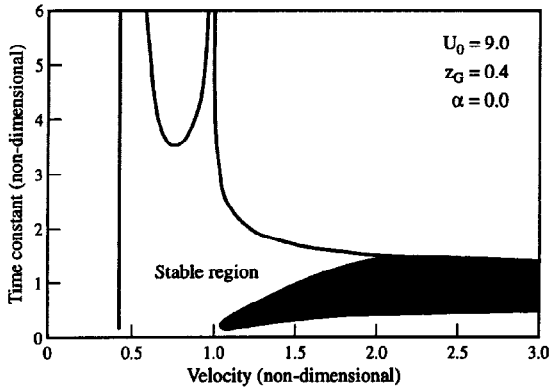

Fig. 14. Loss of stability due to using full vice reduced plane coefficients.

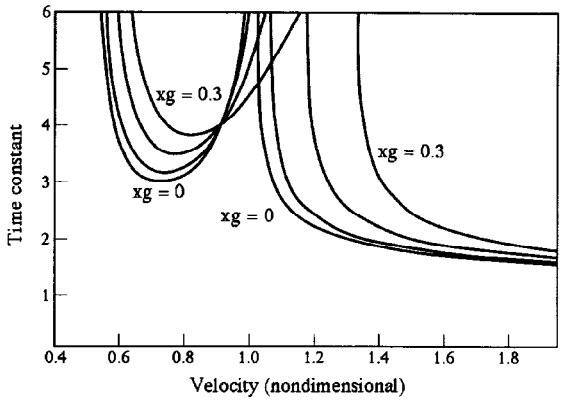

Fig. 15. Bifurcation map for different values of x_{GB}.

to simulations or examine the values of the nonlinear stability coefficient, K, in order to distinguish the response of the model for the different cases.

Figure 14 shows the change in stability for the model with an increase in the control surface coeffcients. The area of lost stability is indicated by the shaded portion of the map, and was obtained through numerical simulations. Calculations of the nonlinear stability coefficient, K, predict that this loss of stability is caused by the shift of the H2 curve from weak-to-moderately supercritical to a strongly subcritical curve. With two strongly subcritical curves in the high-speed region ($U/U_0 > 1$) the possibility of subcritical capture is greatly increased. This effect is confirmed by running an extensive set of simulations and mapping the change from stable to unstable response. We must note that this instability occurs in a region that has four eigenvalues with negative real parts where linear control system design would not predict an instability.

5.3 Trim effects

In order to analyze trim effects, we assume that $x_G \neq x_b$ in the equations of motion [eqns (1) and (2)]. The quantity

$$x_{GB} = x_G - x_b$$

determines the static pitching moment. Without loss of generality, we can assume that the center of buoyancy coincides with the origin of the reference frame, $x_b = 0$. Linearization of the equations of motion, eqns (1) and (2), is now performed in the vicinity of a new equilibrium state which, due to the static pitching moment, differs from the trivial level flight path. If we denote this new equilibrium state by the subscript 0, the linearized equations of motion take the same generic form as eqns (9)–(12), with the additional definitions

$$\begin{aligned}
a_{11}D_v &= (I_y - M_{\dot q})(Z_w - 2C_D A_w U \tan\theta_0) \\
&\quad + (mx_G + Z_{\dot q})(M_w + 2C_D A_w x_A U \tan\theta_0) \\
a_{12}D_v &= (I_y - M_{\dot q})(m + Z_q + 2C_D A_w x_A U \tan\theta_0) \\
&\quad + (mx_G + Z_{\dot q})(M_q - mx_G \\
&\quad - mz_G U \tan\theta_0 - 2C_D A_w x_A U \tan\theta_0) \\
a_{21}D_v &= (m - Z_{\dot w})(M_w + 2C_D A_w x_A U \tan\theta_0) \\
&\quad + (mx_G + M_{\dot w})(Z_w - 2C_D A_w U \tan\theta_0) \\
a_{22}D_v &= (m - Z_{\dot w})(M_q - mx_G - mz_G U \tan\theta_0 \\
&\quad - 2C_D A_w x_A U \tan\theta_0) \\
&\quad + (mx_G + M_{\dot w})(m + Z_q + 2C_D A_w x_A U \tan\theta_0)
\end{aligned}$$

where

$$A_w = \int_0^L b(x)\,dx \tag{53}$$

is the 'waterplane' area, and

$$x_A = \frac{1}{A_w}\int_0^L b(x)x\,dx \tag{54}$$

is its centroid.

The control law is similar to eqn (14) with the addition of a feedforward gain to provide the desired steady-state accuracy

$$\delta = k_1\theta + k_2 w + k_3 q + k_4 z + k_0 \tag{55}$$

The feedback gains are determined as before, whereas the feedforward gain k_0 is based on steady-state accuracy requirements.[20] In order to compute this we set all time derivatives equal to zero, and require that there be no steady-state depth error, i.e. $z_0 = 0$. Therefore, the steady state can be computed from

$$\begin{aligned}
&(Z_w M_\delta - M_w Z_\delta)\tan\theta_0 \\
&\quad + x_{GB}BZ_\delta \cos\theta_0 + z_{GB}BZ_\delta \sin\theta_0 \\
&\quad + C_D A_w (M_\delta - x_A Z_\delta)\tan\theta_0 |\tan\theta_0| = 0
\end{aligned} \tag{56}$$

$$w_0 = U\tan\theta_0 \tag{57}$$

$$q_0 = 0 \tag{58}$$

$$z_0 = 0 \tag{59}$$

The steady-state control effort is computed from

$$\delta_0 = -\frac{1}{Z_\delta}(C_D A_w \tan\theta_0 |\tan\theta_0| + Z_w w_0) \tag{60}$$

and using eqn (55), we compute the feedforward gain as

$$k_0 = \delta_0 - k_1\theta_0 - k_2 w_0 \tag{61}$$

Typical results for the nonzero x_{GB} case are presented in Fig. 15. We can see that as x_{GB} is increased, two Hopf bifurcation branches move towards higher speeds and time constants, and thus increase, in general, the stability region. The third, strongly subcritical, branch remains constant. The other important point we can observe is that the system may become unstable at nominal speed, for high time constants. This is unexpected since we are designing around nominal speed. A more careful examination of the trimmed case, however, shows that the actual forward velocity becomes $\sqrt{u^2 + w^2}$. Therefore, the system may become stable at a value of u other than nominal.

6 CONCLUDING REMARKS

The application of Hopf bifurcation analysis to a submarine design can be an effective tool in the evaluation and modification phases. These methods, when paired with methods that generate hydrodynamic coefficients for a vehicle, will save time, effort and money by reducing the amount of testing necessary to validate a design. Furthermore, this methodology will give the limits of the range of metacentric heights that will maintain stability for the full range of speeds of the design. As was shown, changes in the metacentric height can have a dramatic impact on dynamic stability of motion. Finally, an evaluation of the need for bow planes or forward control surfaces necessary to actually maintain depth control can be undertaken through the use of the coordination coefficient, α, as discussed in the previous section. If the forward planes can be eliminated in a design, a potential source of noise would also be eliminated along with simplifcation of the structure of the control system.

ACKNOWLEDGEMENTS

The authors would like to recognize the financial support of the Naval Postgraduate School Direct Research Fund.

REFERENCES

1. Roddy, R. F., Investigation of the stability and control characteristics of several configurations of the DARPA SUBOFF model (DTRC model 5470) from captive model experiments. David Taylor Research Center, Report DTRC/SHD–1298–08, 1990.
2. Fossen, T. I., Nonlinear modeling and control of underwater vehicles. Doctoral Dissertation, Department of Electrical Engineering, Norwegian Institute of Technology, 1987.
3. Cristi, R., Papoulias, F. A. & Healey, A. J., Adaptive sliding mode control of autonomous underwater vehicles in the dive plane, *IEEE J. Oceanic Engng*, **15** (1991) 3.
4. Goheen, K. R., Jefferys, E. R. & Broome, D. R., Robust self-designing controllers for underwater vehicles. *J. Offshore Mech. Arctic Engng, Trans. ASME*, **109** (1987) 170–8.
5. Gueler, G. F., Modelling, design and analysis of an autopilot for submarine vehicles. *Int. Shipbuilding Prog.*, **36** (1989) 405.
6. Healey, A. J., Model-based maneuvering controls for autonomous underwater vehicles. *J. Dynamic Sys., Measurement and Control, Trans. ASME*, **114** (1992) 614–22.
7. Yoerger, D. R. & Slotine, J.-J. E., Robust trajectory control of underwater vehicles. *IEEE J. Oceanic Engng*, **10** (1985) 4.
8. Guckenheimer, J. & Holmes, P., *Nonlinear Oscillations, Dynamical Systems, and Bifurcations of Vector Fields*. Springer, New York, USA, 1983.
9. Stewart, H. B. & Thompson, J. M. T., Towards a classification of generic bifurcations in dissipative dynamical systems. *Dynamics and Stability of Systems*, **1** (1986) 1.
10. Clayton, B. R. & Bishop, R. E. D., *Mechanics of Marine Vehicles*. Gulf Publishing Company, Houston, TX, USA, 1982.
11. Papoulias, F. A. & Riedel, J. S., Solution branching and dive plane reversal of submarines at low speeds. *J. Ship Res.*, **38** (1993) 3.
12. Papoulias, F. A. & Oral, Z. O., Hopf bifurcations and nonlinear studies of gain margins in path control of marine vehicles. *Appl. Ocean Res.*, **17** (1995) 21–32.
13. Hassard, B. & Wan, Y. H., Bifurcation formulae derived from center manifold theory. *J. Mathematic. Anal. Applicat*, **63** (1978) 297–312.
14. Chow, S.-N. & Mallet-Paret, J., Integral averaging and bifurcation. *J. Differential Equations*, **26** (1977) 112–59.
15. Papoulias, F. A., Guidance and control laws for vehicle pathkeeping along curved trajectories. *Appl. Ocean Res.*, **14** (1992) 291–302.
16. Gertler, M. & Hagen, G. R., Standard equations of motion for submarine simulation. David Taylor Research Center, Report No. 2510, 1967.
17. Friedland, B., *Control System Design: An Introduction to State-space Methods*. McGraw-Hill, New York, USA, 1986.
18. Bateman, C. A., Hopf bifurcation analysis for depth control of submersible vehicles. Master's Thesis, Department of Mechanical Engineering, Naval Postgraduate School, Monterey, CA, USA, 1993.
19. Papoulias, F. A., Dynamics and bifurcations of pursuit guidance for vehicle path keeping in the dive plane. *J. Ship Res.*, **37** (1993) 148–65.
20. Ornek, S., Trim effects on motion stability of submersible vehicles. Master's Thesis, Department of Mechanical Engineering, Naval Postgraduate School, Monterey, CA, USA, 1994.